

Investigation of magnesium-based alloys for biomedical applications

D. Vojtěch^{1*}, H. Čížová¹, K. Volenec²

¹*Department of Metals and Corrosion Engineering, Institute of Chemical Technology, Technická 5, 166 28 Prague 6, Czech Republic*

²*ELLA-CS, Milady Horákové 504, 500 06 Hradec Králové, Czech Republic*

Received 5 May 2006, received in revised form 23 June 2006, accepted 23 June 2006

Abstract

In this work, cast, as well as wrought, Mg-based alloys and pure Mg were investigated as promising materials for construction of biomedical degradable implants. Mg, AZ91, AM50 and MgCa5 alloys were studied. The alloys were prepared by various routes including casting into large sand or small metal moulds and hot extrusion. Microstructures and basic mechanical properties of the alloys were investigated. Chemical properties which are useful to predict the degradation rates of implants were determined by exposition tests in a model saliva solution. It was shown that the microstructures of the wrought materials contained recrystallized grains of α (Mg) phase and intermetallic phases. These microstructures were more uniform than those of the cast alloys which contained more or less continuous network of interdendritic phases around primary α (Mg). The presence of the network led to a reduction of strength of the cast alloys. Exposition tests showed that the cast AZ91Fe0.05 alloy corroded most rapidly in the model saliva. Its corrosion rate was sufficient for medical applications. The fine microstructure of this alloy resulted in a relatively uniform corrosion attack despite the high iron amount.

Key words: biomaterials, mechanical properties, microstructure, corrosion, magnesium

1. Introduction

In medicine, various biomaterials are used for construction of medical implants. The implants are exposed in human body, hence strictly defined properties of applied materials are demanded. These requirements are the most severe in case of implants which are exposed in the human blood. Materials suitable for implants should satisfy following requirements:

- they should be characterized by chemical, mechanical and physical properties which correspond to their function in human body
- they can be sterilized without any change of shape or properties
- their properties should be stable during an exposition to the biological environment (this requirement is not applied to biodegradable implants)
- they must not induce any adverse reactions of a human organism.

Generally, biomaterials can be metallic, polymeric, as well as ceramics, and they are used e.g. for bone, dental or vascular implants. The polymeric biomaterials for some applications can be biodegradable, i.e. they are able to slowly decompose by chemical reactions with components of human environment. The biodegradable implants are of a great importance in applications where a long-term presence of a foreign material initiates undesirable reactions of an organism. The main disadvantage of polymers is a relatively low strength. Therefore, an intensive research in this field has been focused on the metallic biodegradable biomaterials. Magnesium-based alloys appear to be the most promising, because magnesium is characterized by a low toxicity, see Table 1. Moreover, certain magnesium alloys can combine good mechanical properties and sufficient corrosion rate in a human body.

Until present, a number of Mg-based alloys have been considered for medical applications [2–15]:

*Corresponding author: tel.: +421 220 444 290; fax: +420 220 444 400; e-mail address: Dalibor.Vojtech@vscht.cz

Table 1. Toxic doses of different elements (in mg, mg/day or mg/kg of the body weight) in a human body [1]

Element	Toxic dose
Ca	2500 mg/day
Mg	500 mg/day
Fe	20 mg/kg
Mn	11 mg/day
Cu	10 mg
Li	40 mg/kg
Zn	150 mg

1. Mg-Al-Zn (AZ alloys): These materials are widely used in light constructions and hence they are relatively easily commercially available. The alloying leads to a significant improvement of mechanical properties.

2. Mg-Al-RE (AE alloys), Mg-Y-RE (WE alloys) (RE = rare earth metals – Ce, Nd etc.): Alloying with RE metals results in a refinement of microstructure and hence to a significant improvement of strength even at elevated temperatures.

3. Mg-Al-Mn (AM alloys): These alloys show an increased plasticity.

4. Mg-Li-Al, RE, Fe, Y: (LAE, WEL, LE alloys).

5. Mg-Ca: These alloys are considered for fast degradable implant (decomposition during several days of exposure).

Comparison of mechanical properties of the Mg-based alloys with those of the classical metallic biomaterials employed at present, such as Ti alloys, stainless steels and others, is shown in Table 2. It can be seen that the tensile strength, yield strength, modulus of elasticity, as well as elongation, are significantly lower for the Mg-based alloys. From the practical point of view, this means that the biodegradable implants made of magnesium should be designed and constructed in a different way than those of the inert biomaterials. As an example, biodegradable Mg-based stents, i.e. tubular implants which are employed for expansion of e.g. a vessel, esophagus etc., are characterized

by a significantly lower expansion force and maximum elastic deformation as compared to e.g. nitinol stents. Therefore, these stents should be wound of a thicker wire than the nitinol stents and the winding pattern should be also different.

Let us now consider degradation mechanisms of the Mg-based materials. In a human body an implant is mechanically loaded (wear, bending, compression etc.) and also is exposed to various liquid environments. Mechanical degradation is relatively slow and corrosion thus represents the main degradation process. Magnesium alloys are relatively stable in alkaline solutions, as they form a $Mg(OH)_2$ passive layer [1, 19]. The protective effect of this layer grows as the pH is increased. In neutral and particularly acidic solutions magnesium corrodes more rapidly and dissolves which is accompanied with an evolution of hydrogen. In a human body, an implant is mostly exposed to a neutral or slightly acidic solutions containing chlorides and the corrosion of magnesium alloys is strongly accelerated by chloride anions which attack the passive layer. Among alloying elements and impurities, iron, nickel and copper have the most harmful effect on the corrosion resistance of magnesium alloys, even in amounts of the order of 0.01 wt.%. This is due to galvanic cells between fine intermetallic phases rich in Fe, Ni or Cu and Mg matrix. In contrast, rare earth metals show a positive influence on the corrosion resistance of magnesium. The mechanism of corrosion attack and its uniformity are strongly affected also by the microstructure of a particular alloy, i.e. by the type, morphology and distribution of present phases [20–27]. It can be expected that cast and wrought alloys will differ in corrosion behaviour.

The aim of this work is to investigate various wrought and cast Mg-based alloys which have been considered for medical applications. It is very important to describe microstructure of applied materials, because the microstructure strongly influences mechanical properties and also corrosion mechanisms of implants. Knowledge of the degradation mechanisms enables to reduce the risk of human body damage by biodegradable implants [28].

Table 2. Aproximate mechanical properties of various inert biomaterials and Mg-based alloys (UTS – ultimate tensile strength, YS – yield strength, E – modulus of elasticity, ρ – density, UTS/ρ – specific tensile strength, YS/ρ – specific yield strength) [16–18]

Materials	UTS (MPa)	UTS/ρ (MPa·m ³ ·kg ⁻¹)	YS (MPa)	YS/ρ (MPa·m ³ ·kg ⁻¹)	E (GPa)	Elongation (%)
Stainless steel	800	0.10	450	0.06	190	50
Ti alloy	1100	0.24	1000	0.22	110	30
Nitinol Ni-Ti	1500	0.23	–	–	90	25
Co alloy	1200	0.14	1100	0.13	240	55
Mg alloy	300	0.17	300	0.17	40	25

Table 3. Chemical composition (in wt.%) of the investigated alloys measured by XRF

Alloy designation/state	Al	Zn	Si	Cu	Ni	Fe	Mn	Ca
Mg/cast	0.044	0.004	0.048	<0.001	<0.001	<0.001	0.020	0.018
AZ91Fe0.03/cast	9.56	0.864	0.041	<0.001	0.002	0.029	0.106	0.009
AZ91/cast	10.14	1.330	0.033	0.003	<0.001	<0.001	0.014	<0.001
AZ91Fe0.05/cast	10.12	1.050	0.056	<0.001	<0.001	0.046	0.027	0.011
MgCa5/cast	0.042	<0.001	<0.001	<0.001	<0.001	<0.001	0.007	4.750
AZ91(5 mm)/wrought	10.09	0.872	0.107	<0.001	<0.001	0.011	0.066	<0.001
AZ91(50 mm)/wrought	9.93	0.843	0.078	<0.001	<0.001	<0.001	0.096	<0.001
AM50(2.5 mm)/wrought	4.75	0.021	<0.001	<0.001	<0.001	<0.001	0.410	<0.001

2. Experiment

In our experiment we investigated cast, as well as wrought, Mg-based alloys which have already been considered for construction of biodegradable medical implants, e.g. stents, bone implants etc. We investigated pure magnesium, AZ91 (MgAl9Zn1), AM50 (MgAl5Mn) and MgCa5 alloys. Sufficient corrosion rates of these alloys in a human body environment can be expected. The MgCa5 alloy has been considered a material with a very short degradation period in human body (in the order of a few days or weeks). The chemical composition of the studied alloys determined by XRF analysis is shown in Table 3.

The alloys were melted from pure components: Mg (99.7 wt.%, Fe, Ni, Cu contents < 0.001 wt.%), Al (99.99 wt.%), Zn (99.99 wt.%), Ca (99.99 wt.%) and Mn (99.99 wt.%). The AZ91Fe0.03 and AZ91Fe0.05 alloys contained increased iron amount. Due to a very low solubility of pure iron in the liquid magnesium, Al-10wt.%Fe master alloy, instead of the pure iron, was used to achieve the higher levels of Fe. The melting was performed in an induction furnace under argon atmosphere. The investigated alloys were prepared by three routes which resulted in different microstructures:

1. The Mg and AZ91Fe0.03 alloy were prepared by pouring of melt into a sand mould (500 × 200 × 100 mm). The samples (100 × 200 × 20 mm) for further investigation were cut from these castings.

2. The melts (approx. 500 g) of AZ91, AZ91Fe0.05 and MgCa5 alloys were poured into a small (60 × 100 × 10 mm) metal mould. In the metal mould we expected a higher cooling rate than in the preceding case.

3. The AZ91(5 mm), AZ91(50 mm) and AM50(2.5 mm) alloys were prepared in form of rods with diameters 5, 50 and 2.5 mm, respectively. The cylindrical ingots of alloys with diameters of 150 mm were prepared by melting in an induction furnace. The ingots of the AZ91 and AM50 alloys were preheated to 350°C and 300°C, respectively, and then hot extruded at rates between 20–80 cm/s in the hydraulic press. Extrusion ratios were 60, 9 and 50 for the

AZ91(5 mm), AZ91(50 mm) and AM50(2.5 mm), respectively.

The samples cut from the castings and rods were subject to metallographic treatment including mounting, grinding and polishing. Optical microscope (Olympus PMEU), as well as SEM (Hitachi S 450) with EDS (Kevex Delta 5) analyser, were used for structural examinations. The samples were etched in 3% solution of nitric acid in ethanol. In order to determine mechanical properties of the studied materials, hardness measurements (HV 1, 10 measurements on each sample) and tensile tests (5 measurements on each sample) were realized. Rod samples (6 mm in diameters and 90 mm in length) of the cast alloys and wrought AZ91(50 mm) alloy for tensile tests were prepared by turning. Samples of the wrought AZ91(5 mm) and AM50(2.5 mm) alloys were cut from original rods to appropriate length of 90 and 40 mm, respectively. Tensile tests were performed on a loading machine FPZ100/1 at a loading rate of 3 mm/min. As was stated before, implants in a human body can be exposed to various water solutions, hence we had to choose an appropriate model solution for exposition corrosion tests. A solution of model saliva, which is useful to estimate corrosion behaviour of e.g. esophageal stents, was chosen for our corrosion testing. This solution contained 0.4 g/l NaCl, 0.4 g/l KCl, 0.795 g/l CaCl₂·2H₂O, 0.690 g/l NaH₂PO₄·H₂O, 0.3 g/l KSCN and 1 g/l urea [29]. The exposition tests (4 tests with each investigated alloy) were performed according to ASTM G31-72. Each sample was exposed in the model saliva at 20°C and the ratio of solution volume (in cm³) to the sample surface (in cm²) was equal to 50. In order to simulate a movement of saliva, the solution was periodically (after 48 hours exposition) replaced by a fresh solution. The total exposition period was 168 hours, except for the MgCa5 alloy which was exposed only 24 hours. Corrosion rate (in mm/year) was computed from weight loss after removing corrosion products from the sample surface using a water solution according to ČSN ISO 8407 (1000 ml of the solution contained 200 g CrO₃, 10 g AgNO₃, 20 g Ba(NO₃)₂ and water). Beside the total corrosion rate, the mechanism of corrosion attack is important

for medical implants. As an example, an implant is not acceptable if small and sharp pieces are evolved during corrosion. Such pieces can penetrate the tissue and damage a patient. Therefore, it was important for us to determine whether corrosion proceeded uniformly or was localized in a certain part of material. After the exposition tests, the surface of samples was studied in cross-section.

3. Results and discussion

3.1. Microstructures

Microstructures of the Mg and AZ91Fe0.03 alloy which were cast into a large sand mould are shown in Figs. 1, 2. Both microstructures are coarse due to a slow cooling of melts in the mould.

The Mg comprises coarse equiaxed grains (average grain size more than $500\ \mu\text{m}$), see Fig. 1. Since the total content of impurities is very small in this alloy

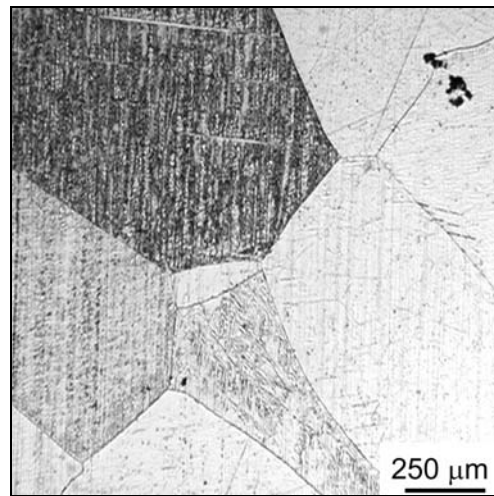


Fig. 1. Optical micrograph of the Mg.

(in order of a few hundredths of wt.%), see Table 3, intermetallic phases rich in these elements were not

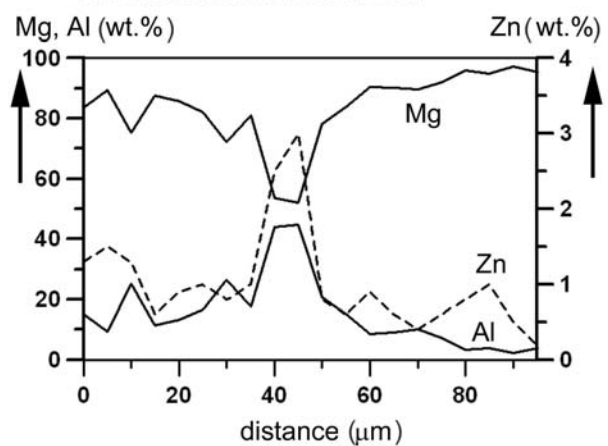
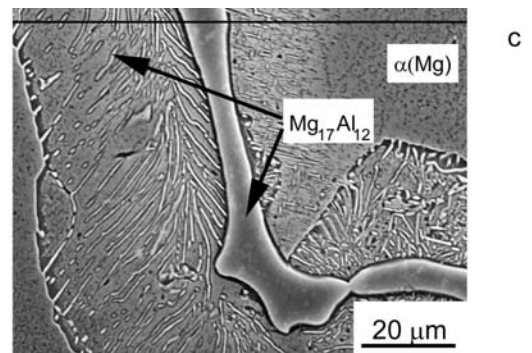
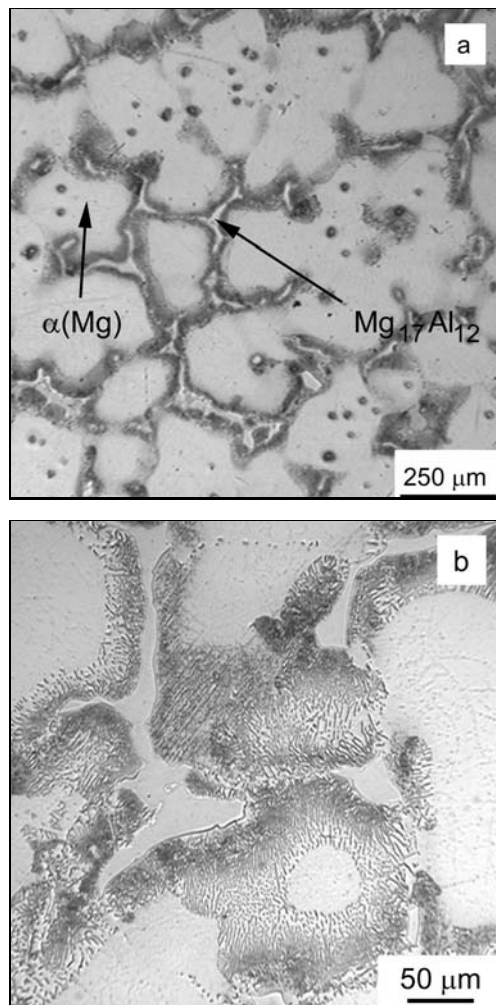


Fig. 2. Microstructure of the AZ91Fe0.03 alloy: a), b) optical micrographs, c) SEM micrograph with concentration profiles of Al, Zn, Mg along a drawn line.

found in the microstructure. It can be assumed that a large portion of impurities is dissolved in Mg-based solid solution and that the volume fraction of intermetallics is very low.

Optical and SEM micrographs of the AZ91Fe0.03 alloy are shown in Figs. 2a–c. An overall view in Fig. 2a illustrates that the microstructure is heterogeneous and is composed of primary $\alpha(\text{Mg})$ dendrites with branches of approx. $200\ \mu\text{m}$ in diameter and of intermetallic phases localized mainly along the dendrite boundaries. A more detailed optical micrograph in Fig. 2b reveals an internal substructure in the vicinity of dendrite boundaries. It can be seen that this region contains a fine mixture of intermetallic particles in Mg-based matrix. SEM micrograph of this region, together with concentration profiles of Al, Zn and Mg along a drawn line, see Fig. 2c, show that the irregular particles at dendrite boundaries correspond to the $\text{Mg}_{17}\text{Al}_{12}$ phase. Zinc dissolves in this phase to some extent (approx. 3 wt.% Zn). It can be assumed that the $\text{Mg}_{17}\text{Al}_{12}$ phase forms as a result of non-equilibrium solidification. Due to the dendritic segregation, the last portion of melt enriched in Al solidifies as a non-equilibrium eutectic $\alpha(\text{Mg}) + \text{Mg}_{17}\text{Al}_{12}$. Eutectic $\alpha(\text{Mg})$ phase becomes a part of the primary dendrites and the $\text{Mg}_{17}\text{Al}_{12}$ phase forms nearly continuous network. The dark regions in Figs. 2a,b surrounding the $\text{Mg}_{17}\text{Al}_{12}$ phase are direct consequence of the dendritic segregation, as they contain increased amounts of Al, see Fig. 2c. The chemical microanalysis proves that this is a fine mixture composed mainly of $\text{Mg}_{17}\text{Al}_{12}$ phase and $\alpha(\text{Mg})$ solid solution. Most likely, this mixture is formed by a decomposition of peripheral parts of primary dendrites, originally rich in Al, during cooling to the room temperature. The AZ91Fe0.03 alloy contains about 0.03 wt.% Fe. The distribution of iron is very important from the viewpoint of corrosion behaviour. Although the chemical microanalysis was performed very carefully, we did not find any intermetallic particles rich in Fe. This is due to very low iron concentration in the alloy which results in a very small volume fraction of these phases. Moreover, iron was not observed to be concentrated either in the $\text{Mg}_{17}\text{Al}_{12}$ phase or in primary dendrites.

Figures 3–5 show optical and SEM micrographs of the AZ91, AZ91Fe0.05 and MgCa5. These alloys were cast into small metal mould, hence they are characterized by much finer microstructure as compared to the alloys prepared in form of large castings.

The AZ91 alloy is illustrated in Fig. 3a. The microstructure comprises primary $\alpha(\text{Mg})$ dendrites and a network of $\text{Mg}_{17}\text{Al}_{12}$ phase. The average diameter of dendritic branches is about ten times lower than that of the AZ91Fe0.03 alloy, see also Fig. 2a. The AZ91 and AZ91Fe0.03 alloys differ also in the volume fraction of two-phase dark regions along the dendrite boundaries. In the more rapidly solidified alloy (AZ91)

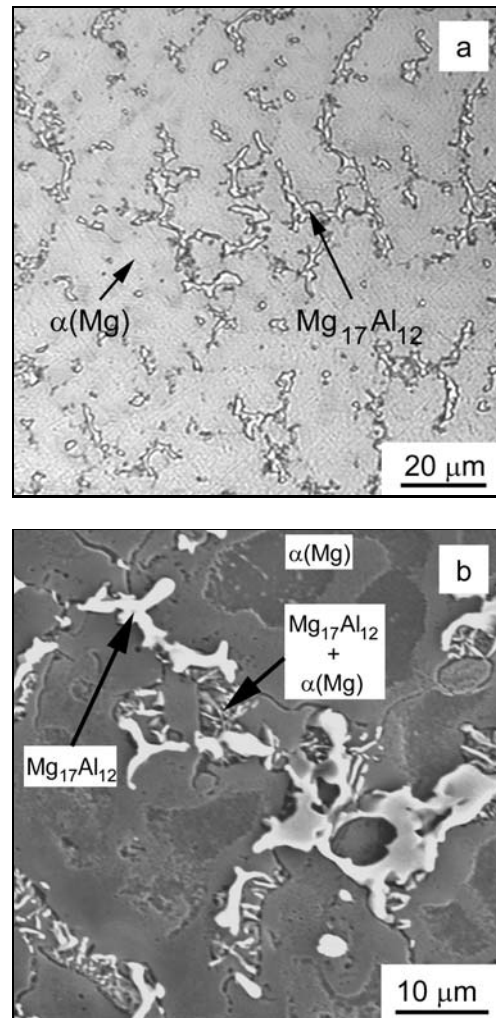


Fig. 3. Microstructure of the AZ91 alloy: a) optical micrograph, b) SEM micrograph.

these regions occupy a lower portion of microstructure and the interdendritic $\text{Mg}_{17}\text{Al}_{12}$ phase is mostly directly surrounded by homogeneous dendrites, as is seen in a SEM micrograph in Fig. 3b. As was stated before, these heterogeneous areas result from decomposition of $\alpha(\text{Mg})$ solid solution. In a large casting where the cooling is slow, decomposition can proceed, because a sufficient time is available for Al and Mg diffusion. On the other hand, in a small casting prepared in metal mould the cooling rate is much higher and aluminium rather remains in solid solution based on Mg.

Microstructure of the AZ91Fe0.05 alloy is similar to the preceding one, see Fig. 4a. It is again composed of $\alpha(\text{Mg})$ dendrites and a network of $\text{Mg}_{17}\text{Al}_{12}$ phase. The increased iron amount does not affect the distribution of main components of the alloy. Detailed SEM investigation and chemical microanalysis of regions in the vicinity of dendrites boundaries revealed the same elements distribution like in the case of the AZ91 alloy, see Fig. 3b. The chemical microanalysis was also

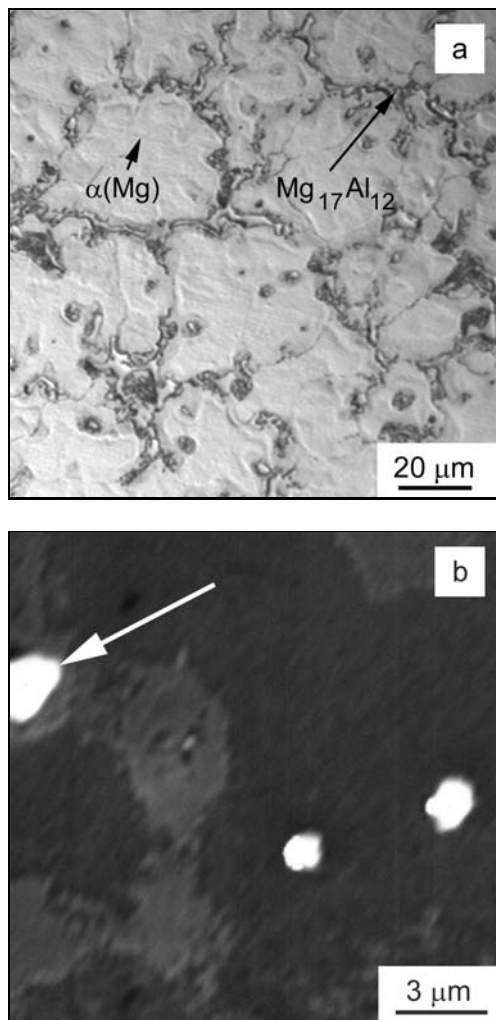


Fig. 4. Microstructure of the AZ91Fe0.05 alloy: a) optical micrograph, b) detailed SEM micrograph showing Fe-rich particles in dendritic cores (light, marked by an arrow).

focused on the determination of iron distribution in the alloy. This measurement shows that iron is not present either in regions near the grain boundaries or in interdendritic $\text{Mg}_{17}\text{Al}_{12}$ phase. Surprisingly, careful analysis identifies very fine iron-rich particles concentrated in dendritic cores, see light particles in Fig. 4b. These particles are only about a few μm in diameter and beside iron they contain also an increased amount of aluminium. As an example, a particle indicated by an arrow in Fig. 4b contains 47.1 at.% Mg, 44.7 at.% Al, 7.0 at.% Fe and 0.4 at.% Zn. The presence of Mg in the particle is not probable, as magnesium and iron do not form intermetallic phases [30]. The measured Mg concentration is rather due to surrounding Mg matrix. Most likely, the Fe-rich phase is based on FeAl_6 system and its composition corresponds to the FeAl_6 phase. If we take into account the fact that iron was added in form of the Al-Fe master alloy, the occurrence of such phases is not sur-

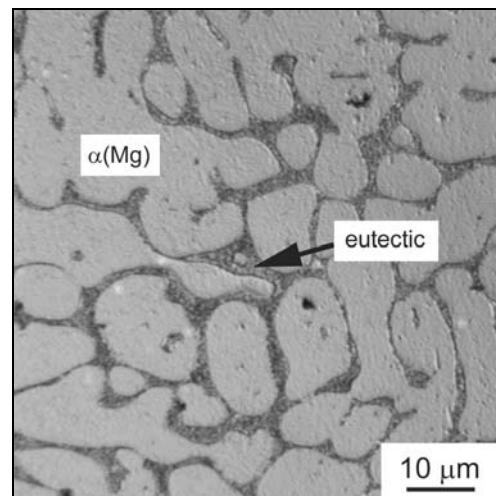


Fig. 5. Optical micrograph of the MgCa5 alloy.

prising. During melting of the alloy, the Al and Fe are dispersed in the melt. Upon cooling the Fe-Al phases solidify first, as they are characterized by the highest melting point [30]. Then they are surrounded by primary $\alpha(\text{Mg})$ dendrites. This is the reason why the iron-rich particles are identified in the dendritic cores.

Optical micrograph of the MgCa5 alloy is shown in Fig. 5. It is composed of primary dendrites (light) and eutectic (dark). The chemical microanalysis proved that the eutectic is enriched in calcium and, according to the Mg-Ca phase diagram [30], it comprises two phases – $\alpha(\text{Mg}) + \text{Mg}_2\text{Ca}$. It can be assumed that the Ca-rich eutectic will be first attacked by a corrosion agent, see later.

Microstructures of the wrought AZ91(5 mm), AZ91(50 mm) and AM50(2.5 mm) alloys in cross, as well as longitudinal sections, are shown in Figs. 6–8. Due to the hot extrusion, the as-cast microstructure vanishes and the $\alpha(\text{Mg})$ solid solution forms equiaxed fully recrystallized grains. These grains do not show any deformation texture.

The AZ91(5 mm) alloy is illustrated by optical micrographs in Fig. 6. Besides the recrystallized $\alpha(\text{Mg})$ grains of about 20 μm in diameter, the structure contains also fine particles of the $\text{Mg}_{17}\text{Al}_{12}$ phase. These particles are formed by fragmentation of a network originally present in the as-cast microstructure, see also Figs. 2a and 3a, due to extrusion. In the cross-section, see Fig. 6a, the $\text{Mg}_{17}\text{Al}_{12}$ particles are not distributed uniformly and occupy mostly the boundaries of recrystallized grains. In the longitudinal section, however, the Al-rich particles show an arrangement corresponding to direction of the hot extrusion, as shown in Fig. 6b. It can be assumed that the $\text{Mg}_{17}\text{Al}_{12}$ particles are not ductile at the relatively low extrusion temperatures, hence they arrange into rows parallel to the

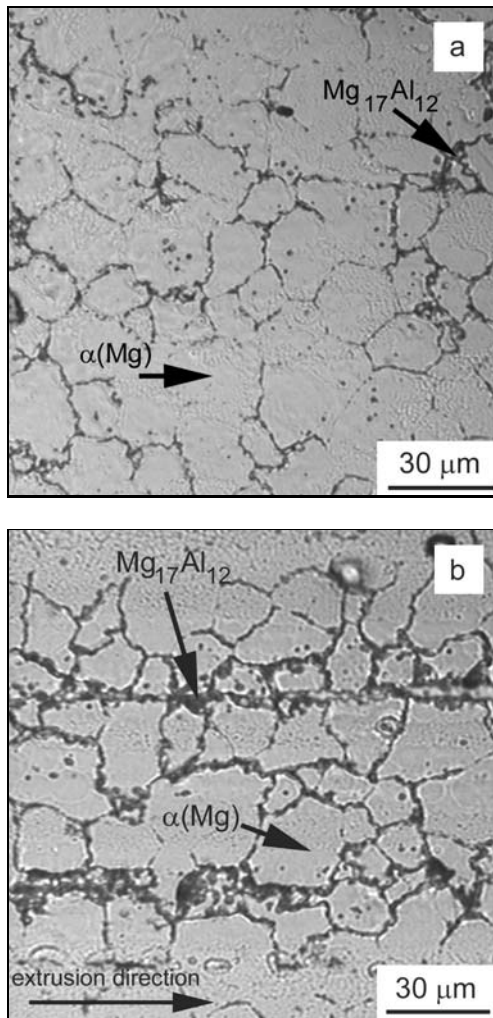


Fig. 6. Optical micrographs of the AZ91(5 mm) alloy: a) cross-section, b) longitudinal section.

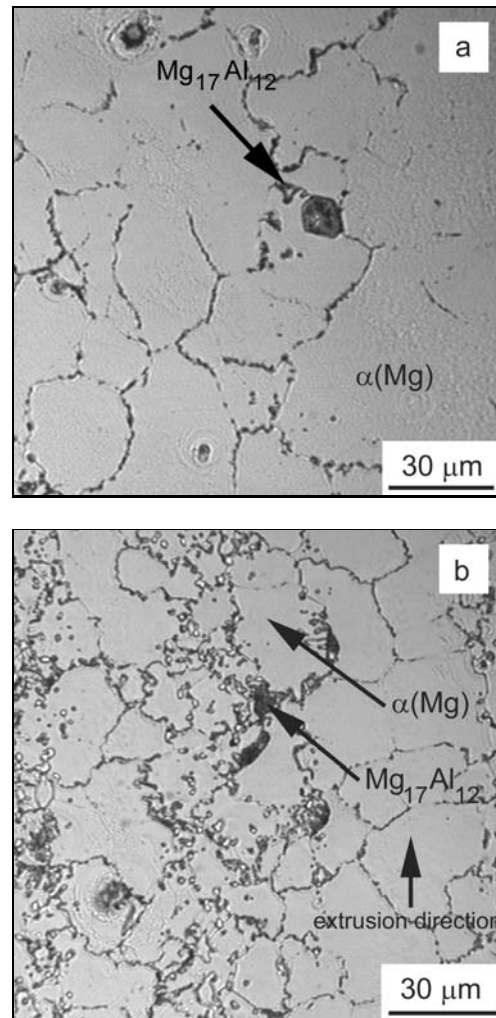


Fig. 7. Optical micrographs of the AZ91(50 mm) alloy: a) cross-section, b) longitudinal section.

extrusion direction, instead of being deformed. A careful chemical microanalysis of the alloy did not prove any Zn-rich particles, instead of it, zinc is distributed uniformly throughout the alloy volume.

Microstructure of the AZ91(50 mm) is similar to the preceding one, except for difference in dimensions of the $Mg_{17}Al_{12}$ particles rows, see Figs. 7a,b. The extrusion ratio was much lower for the 50 mm rod than for the 5 mm rod and hence the rows of intermetallic particles are significantly thicker in this case, compare Figs. 7b and 6b.

The last alloy which was investigated in our study was the wrought AM50(2.5 mm) alloy. An optical micrograph in a longitudinal section in Fig. 8a reveals presence of three structural components: recrystallized fine grains of $\alpha(Mg)$ solid solution (light) with average diameter of approx. $10 \mu m$, very fine particles aligned into rows parallel to the rod axis and relatively coarse particles which do not show any apparent

arrangement. The nature of the intermetallic phases was determined by chemical microanalysis and X-ray mapping. The results are illustrated in Fig. 8b where a SEM micrograph together with Mg, Al and Mn distributions is shown. It can be observed that the fine particles correspond to the $Mg_{17}Al_{12}$ phase whose behaviour during extrusion is the same as in the AZ alloys. On the other hand, the coarse particles are rich in Mn and Al. The chemical microanalysis of several particles was performed and following concentrations were obtained: Mn 44–48 at.%, Al 45–52 at.% and Mg 1–4 at.%. If we consider the Al-Mn equilibrium phase diagram, these particles correspond most likely to an intermetallic phase which is sometimes denoted as Al_3Mn_5 [30]. In the phase diagram, however, this phase occurs in a relatively wide concentration range which implies that Al atoms in the crystal lattice can be in part substituted by Mn and vice-versa, and probably also by Mg to a certain extent.

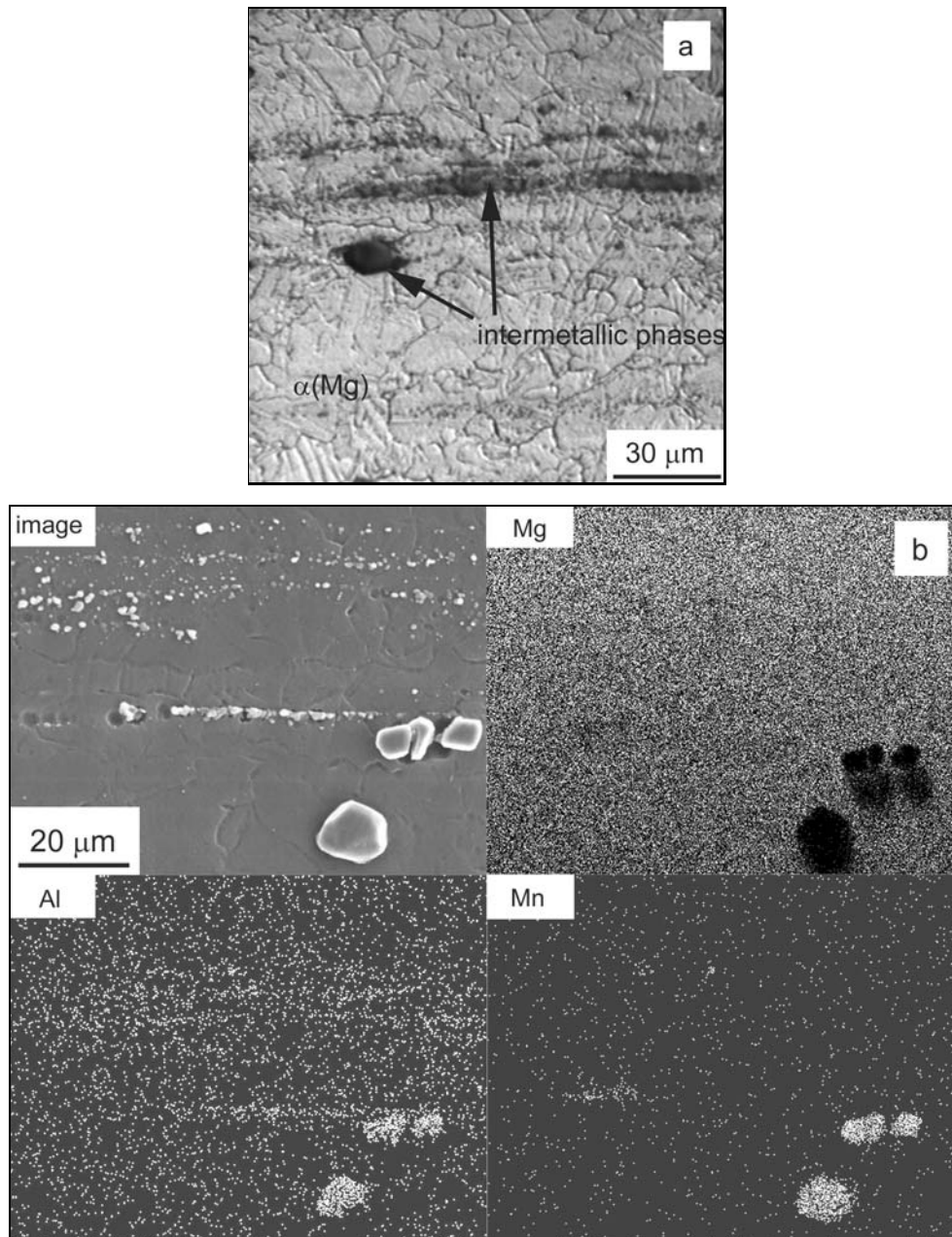


Fig. 8. Microstructure of the AM50(2.5 mm) alloy: a) optical micrograph in a longitudinal section, b) SEM micrograph with X-ray maps of Mg, Al and Mn distributions.

3.2. Mechanical properties

Microstructures described in the preceding chapter strongly affect the mechanical properties of materials. The knowledge of mechanical properties facilitates to find an appropriate material for a particular application and also to design its shape. Basic information on mechanical behaviour of any material is obtained from hardness and tensile tests.

Vickers hardness of the investigated materials is compared in Fig. 9. As expected, the Mg shows the lowest hardness (approx. 30 HV 1) of all investigated

materials which is primarily due to very small contents of others elements, see Table 3. In contrast, the hardness of the wrought AM50(2.5 mm) alloy and cast AZ91, AZ91Fe0.05, MgCa5 alloys is approx. 70 HV 1, more than double that of the pure Mg. The remaining materials, i.e. wrought AZ91(5 mm), AZ91(50 mm) and cast AZ91Fe0.03 alloy, exhibit slightly lower hardness levels of about 60–65 HV 1 but this difference is not very significant.

Generally, the hardening of cast and hot extruded alloys can be described mainly by three contributions [31, 32]:

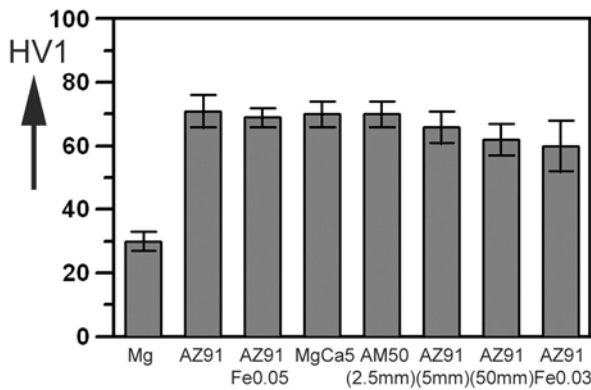


Fig. 9. Vickers hardness HV 1 of the investigated materials.

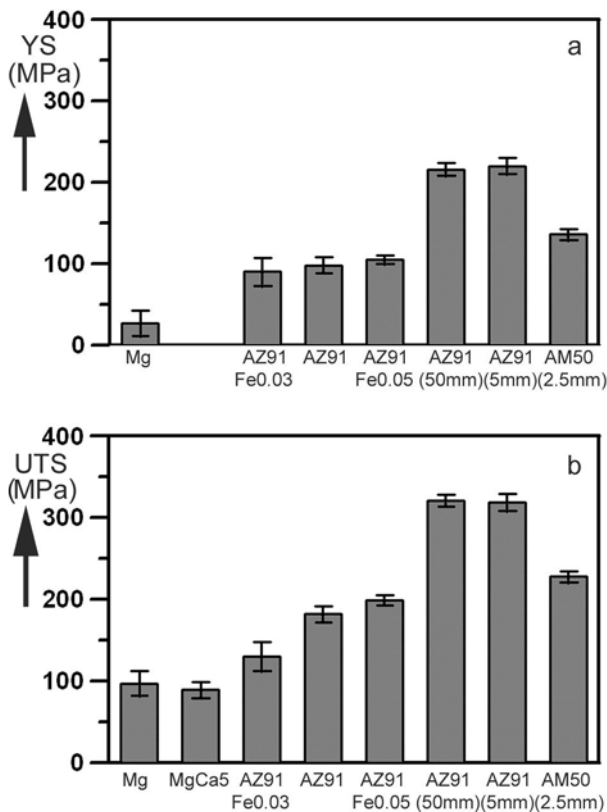


Fig. 10. Yield strength (YS) (a) and ultimate tensile strength (UTS) (b) of the investigated materials.

1. Hall-Petch hardening due to grain boundaries,
2. Orowan hardening due to non-coherent particles of intermetallic phases and
3. solid solution hardening.

Hardening due to coherent or semicoherent precipitates is neglected, as the alloys were not heat treated. The high hardness of the cast AZ91 and AZ91Fe0.05 alloys is a result of the high aluminium contents and fine microstructures, see Figs. 3 and 4. Aluminium leads to formation of hard and brittle in-

termetallics, mainly the $Mg_{17}Al_{12}$ one. These intermetallics act as obstacles for dislocation slip. As the phase is non-coherent with the Mg matrix [30], the Orowan mechanism operates here. Additionally, the atomic radii of Al and Mg are 1.43 Å and 1.60 Å [30], respectively. If some Mg atoms in the $\alpha(Mg)$ phase are substituted by Al atoms, the discrepancy between atomic radii results in a stress in Mg lattice which can then suppress slip of dislocations. This solid solution hardening contribution is proportional to the Al content in the $\alpha(Mg)$ phase [32]. The chemical microanalysis proved that the Al content in the $\alpha(Mg)$ phase in both AZ91 and AZ91Fe0.05 alloy varies between approx. 2 wt.% (dendritic cores) and 10 wt.% (vicinity of the interdendritic phase). Finally, the relatively small dimensions of $\alpha(Mg)$ dendrites contribute to the Hall-Petch hardening, as the dendrite boundaries suppress the dislocation slip. Similar three hardening mechanisms as stated above operate in the MgCa5 and AM50(2.5 mm) alloys. In the former one the Orowan hardening is caused by the eutectic Mg_2Ca phase, see Fig. 5. Since the amount of Ca (atomic radius of 2 Å [30]) in the $\alpha(Mg)$ phase was proved to vary between 1 and 5 wt.%, some solid solution hardening can be also expected. In the case of the wrought AM50(2.5 mm) alloy the high hardness results mainly from the fineness of $\alpha(Mg)$ grains and Al-rich particles, see Fig. 8. The slightly lower hardness of the wrought AZ91(5 mm) and AZ91(50 mm) alloys as compared to the AZ91 and AZ91Fe0.05 ones may be a consequence of a lower volume fraction of the $Mg_{17}Al_{12}$ intermetallic phase. It can be expected that a part of this phase dissolves in the $\alpha(Mg)$ solid solution upon heating before and during the hot extrusion. The reason of the lower hardness of the AZ91Fe0.03 alloy is its coarse microstructure in comparison with both AZ91 and AZ91Fe0.05 alloy.

Comparison of yield strength (YS) and ultimate tensile strength (UTS) of the investigated materials is shown in Figs. 10a,b. As expected, the wrought alloys, particularly the AZ91 ones, exhibit the highest strength. This is due to the high Al content, and also due to their fine, homogeneous microstructure and relatively uniform distribution of intermetallic phases, see Figs. 6–8. It can be also expected that the extrusion process eliminates casting defects like shrinkage cavities. On the other hand, presence of the semicontinuous network of brittle interdendritic phases in all cast AZ91 alloys, see Figs. 2–4, leads to a reduction of tensile strength. This network facilitates the propagation of fracture cracks. In the case of the cast MgCa5 alloy, see Fig. 5, the eutectic network is almost continuous and hence the ultimate tensile strength of this material is similar to the pure Mg. Moreover, plastic deformation was not observed in this case, so yield strength was not determined.

From the mechanical properties viewpoint, the

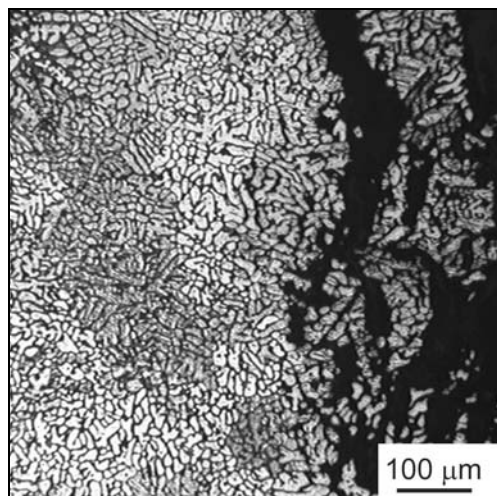
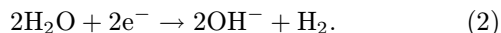
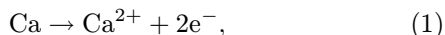


Fig. 11. Optical micrograph of the cross-sectioned corroded surface of the MgCa5 alloy after 24 hours exposition in the model saliva at 20°C.

wrought AZ91(5 mm), AZ91(50 mm) and AM50(2.5 mm) alloys seem to be the most convenient for construction of mechanically loaded implants, like e.g. stents. The AZ91 and AZ91Fe0.05 alloys which were cast into small metal mould and which thus have fine and homogeneous structure are also promising, as the casting permits to simply produce implants of relatively complicated shapes, e.g. bone implants.

3.3. Corrosion properties

As was stated before, corrosion can be considered the main degradation process of biodegradable implants. The exposition tests showed that the corrosion rate of the MgCa5 alloy was 60 ± 18 mm/year which is 1–2 orders of magnitude higher value as compared to the other materials. After 24 hours exposition in the model saliva the samples appeared white and strongly corroded. Small bubbles of evolving hydrogen were also observed on the sample surface. As was already given, the MgCa5 alloy is investigated as it seems to be prospective for fast degradable implants. The main reason for such a high corrosion rate is the large amount of calcium in this alloy. It can be assumed that calcium or calcium-rich phases readily react with the water solution which is accompanied with hydrogen evolution, according to following equations:



This mechanism is supported also by Fig. 11 where a selective corrosion of Ca-rich eutectic and a total disintegration of the material can be seen.

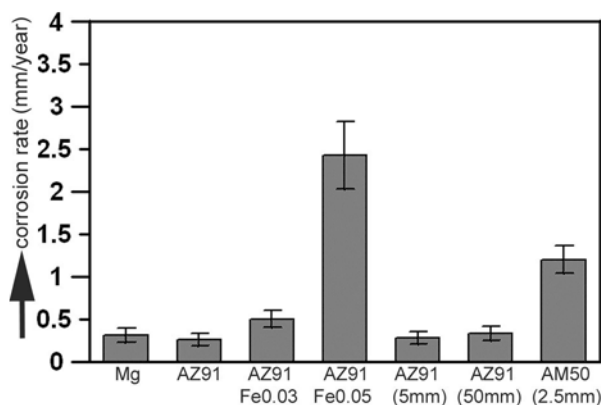
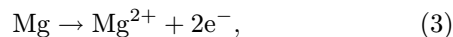
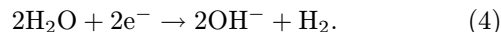


Fig. 12. Corrosion rates of the investigated materials in the model saliva solution at 20°C.

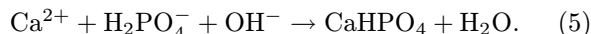
Corrosion rates of the other investigated materials in the model saliva are summarized in Fig. 12. It should be noted that after all tests the surface of samples was covered with a light (nearly white) layer of corrosion products which contained mainly Ca, P and O. XRD analysis proved the presence of calcium hydrogen phosphate dihydrate ($\text{CaHPO}_4 \cdot 2\text{H}_2\text{O}$) as the main constituent of the corrosion products on all samples. It can be thus assumed that the corrosion process includes an anodic reaction:



and a cathodic reaction [33, 34]:



An increase of solution pH due to the cathodic reaction was confirmed by direct measurement. This increase led to precipitation of $\text{CaHPO}_4 \cdot 2\text{H}_2\text{O}$ from the model saliva solution originally containing both Ca^{2+} and $\text{H}_2\text{PO}_4^{-}$ ions:



In order to determine the corrosion rate, the corrosion products had to be removed in appropriate solution, see experimental part. It can be seen in Fig. 12 that the Mg, AZ91, AZ91Fe0.03, AZ91(5 mm) and AZ91(50 mm) corrode at similar rates of approximately 0.3–0.5 mm/year. It means that the degradation of e.g. a tubular implant with the wall thickness of 0.5 mm would take more than one year. Such a rate is too small and unacceptable for practical applications in degradable implants. The observed similarity of corrosion rates implies that neither aluminium content nor preparation route affects corrosion process significantly. It can be assumed that Al in part incorporates into the surface layer of corro-

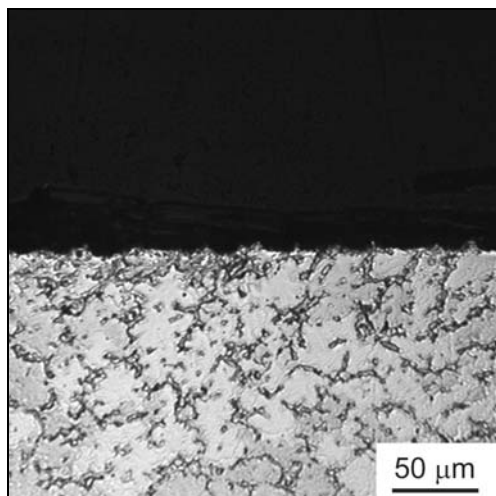


Fig. 13. Optical micrograph of the cross-sectioned corroded surface of the AZ91 alloy after 168 hours exposure in the model saliva at 20°C.

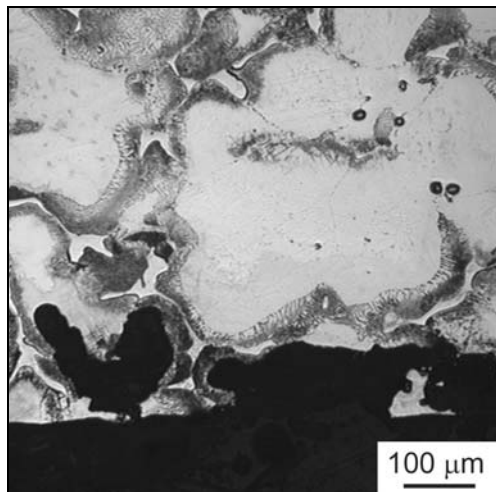


Fig. 14. Optical micrograph of the cross-sectioned corroded surface of the AZ91Fe0.03 alloy after 168 hours exposure in the model saliva at 20°C. Localized corrosion attack preferentially on the $\alpha(\text{Mg})$ phase is seen.

sion products [33, 35] but this effect in nearly neutral solution of the model saliva is negligible. Similarly, the more uniform as-wrought microstructure should reduce the corrosion rate but this was not proved, either. From this viewpoint, the model saliva seems to be not very aggressive medium for the materials given above. This is mainly due to its nearly neutral pH and due to a relatively low chloride concentration. The chloride concentration is the main factor affecting the corrosion rate in neutral solutions. As an example, it was reported [35] that the corrosion rate of the AZ91 alloy in 1M NaCl is higher than the values given above by approx. two orders of mag-

nitude. The cross-sections of the corroded surfaces after removal of corrosion products were examined in detail and only a small roughness of all surfaces was observed, as is illustrated for the AZ91 alloy in Fig. 13, which implies a relatively uniform corrosion. Only one exception of this behaviour was found – the AZ91Fe0.03 alloy. By a careful observation of this alloy we found a few sites with a local and deep corrosion attack preferentially on the $\alpha(\text{Mg})$ phase, see Fig. 14. This localized attack may be a result of iron-rich particles in the structure. These particles were not found by microstructural examination due to a very low volume fraction but their presence is likely, as iron is practically insoluble in solid magnesium [30]. In the vicinity of a Fe-rich particle, a galvanic cell between this particle and the $\alpha(\text{Mg})$ phase, as a less noble structural component in the alloy, forms [2]. The galvanic cells result from a difference between electrochemical behaviour of a more noble Fe-rich phase and less noble $\alpha(\text{Mg})$ phase. As a result, the preferential and rapid corrosion of the $\alpha(\text{Mg})$ phase occurs in this site. Since the number of Fe-rich particles in the alloy is very small, the total corrosion rate is not influenced significantly, see Fig. 12.

In contrast to the preceding alloys, corrosion rate of the AM50(2.5 mm) and particularly that of the AZ91Fe0.05 alloy is significantly higher. In the latter case, influence of the increased iron amount plays a dominant role. As was stated above, the iron-rich particles in the structure, see Fig. 4b, form galvanic cells with the $\alpha(\text{Mg})$ matrix which thus accelerate its corrosion. Since the microstructure of the AZ91Fe0.05 alloy is fine and the distribution of dispersed Fe-rich particles is relatively uniform throughout the volume of the alloy (Fig. 4), the corrosion proceeds without the formation of the local and deep holes on the surface, see Fig. 15a, in contrast to the AZ91Fe0.03 alloy (Fig. 14). The increased corrosion rate of the AM50(2.5 mm) alloy is probably also a result of galvanic cells between Al-Mn phases which were identified in the structure, see Fig. 8, and $\alpha(\text{Mg})$ matrix. However, in contrast to the preceding material, the Al-Mn particles are coarser and their distances are significantly larger than those of the Fe-rich particles. Therefore, corrosion process leads to formation of more localized and relatively deep holes in the material, see Fig. 15b.

If we compare the investigated alloys, the cast AZ91Fe0.05 alloy seems to be most suitable for preparation of medical degradable implants. Its main advantages are: fine structure and hence fine distribution of “corrosion accelerating” Fe-rich phases. These factors limit the danger of undesirable separation of sharp pieces of material during degradation which could penetrate to other parts of a human body and cause a damage.

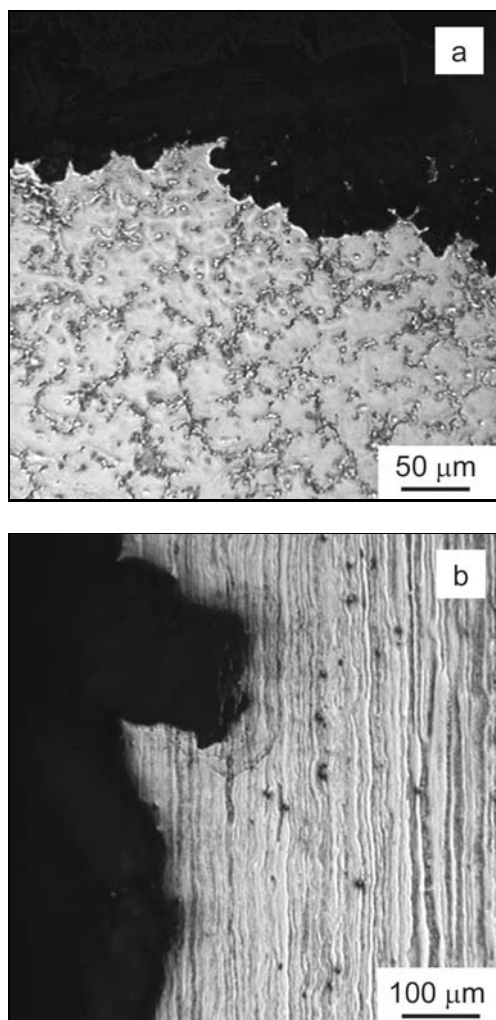


Fig. 15. Optical micrographs of the cross-sectioned corroded surface after 168 hours exposition in the model saliva at 20°C: a) AZ91Fe0.05 alloy, b) AM50(2.5 mm) alloy.

4. Summary

In this work, seven cast, as well as wrought, Mg based alloys and pure Mg were investigated as promising materials for construction of biomedical degradable implants. The work was focused on the AZ91, AM50 and MgCa5 alloys. Microstructures, mechanical and chemical properties were examined. It was shown that the structures of wrought materials were more uniform as compared with cast ones. The cast alloys contained more or less continuous network of interdendritic phases which led to a reduction of ultimate tensile strength. The fine microstructure of alloys cast into a small metal mould, however, can lead to a sufficient strength of implants of complicated shapes. Simple corrosion exposition tests showed that the AZ91Fe0.05 alloy which was prepared by casting into a small metal mould exhibited a sufficient corrosion rate due to the high Fe content. The fine micro-

structure of this alloy resulted in a rapid but relatively uniform corrosion attack which is important from the medical viewpoint.

Acknowledgements

This work was financially supported by research programmes MSM 6046137302 and FI-IM2/108. Authors would like to thank to Dr. Maisnar from Magalco company which provided some of the investigated materials.

References

- [1] VOJTĚCH, D.: Stents production from biodegradable Mg alloys. Research report for ELLA-CS, Prague, Institute of Chemical Technology 2004 (in Czech).
- [2] KAINER, K. U.: Magnesium Alloys and Technologies. Weinheim, Wiley-VCH Verlag GmbH 2003.
- [3] WINDHAGEN, H.—WITTE, F.: patent no WO03055537, 2003.
- [4] HAUSDORF, G.—HEUBLEIN, B.: patent no US2002004060, 2002.
- [5] MEYER-LINDENBERG, A.—NIEMEYER, M.: patent no WO02100452, 2002.
- [6] DI MARIO, C.—GRIFFITHS, H.: Journal of Interventional Cardiology, 17, 2004, p. 391.
- [7] HEUBLEIN, B.—ROHDE, R.: Heart, 89, 2003, p. 651.
- [8] HAFERKAMP, H.—KAESE, V.: In: Proceedings 2nd Israeli International Conference on Magnesium Science and Technology. Eds.: Agnion, E., Eliezer, D. MRI, Dead Sea, 2000, p. 159.
- [9] LÉVESQUE, J.—DUBÉ, D.: Mater. Sci. Forum, 426–432, 2003, p. 521.
- [10] GEROLD, B.: patent no US2004098108, 2004.
- [11] KIM, J. M.—PARK, B. K.: Mater. Sci. Forum, 486–487, 2005, p. 424.
- [12] CHEN, R. S.—BLANDIN, J. J.: Mater. Sci. Forum, 488–489, 2005, p. 275.
- [13] CHOI, B. H.—YOU, B. S.: Mater. Sci. Forum, 475–479, 2005, p. 2477.
- [14] LIU, M.—WANG, Q.: Mater. Sci. Forum, 488–489, 2005, p. 763.
- [15] WITTE, F.—KAESE, V.: Biomaterials, 26, 2005, p. 3557.
- [16] PONCIN, P.—PROFT, J.: In: Proceedings Materials & Processes for Medical Devices Conference. Ed.: Sanjay Shrivastava. Materials Park, ASM International 2003, p. 266.
- [17] ASM Handbook, Volume 2, Properties and Selection: Nonferrous Alloys and Special-Purpose Materials. Materials Park, ASM International 1990.
- [18] HEUBLEIN, B.—HAUSDORF, G.: patent no EP155-2856, 2005.
- [19] ASM Handbook, Volume 13, Corrosion. Materials Park, ASM International 1992.
- [20] SONG, G.—ATRENS, A.: Cor. Sci., 39, 1998, p. 1769.
- [21] MATHIEU, S.—RAPIN, C.: Cor. Sci., 45, 2003, p. 2741.
- [22] MATHIEU, S.—RAPIN, C.: Cor. Sci., 44, 2002, p. 2737.

- [23] BONORA, P.—ANDREI, M.: *Cor. Sci.*, 44, 2002, p. 729.
- [24] INOUE, H.—SUGAHARA, K.: *Cor. Sci.*, 44, 2002, p. 603.
- [25] KHASELEV, O.—YAHALOM, J.: *Cor. Sci.*, 40, 1998, p. 1149.
- [26] AUNG, N. N.—ZHOU, W.: *J. Appl. Electrochem.*, 32, 2002, p. 1397.
- [27] GURMAN, E. M.: *J. Mat. Synt. Proc.*, 8, 2000, p. 133.
- [28] VOJTĚCH, D.: unpublished results.
- [29] DUFFO, G. S.—CASTILLO, E. Q.: *Corrosion*, 60, 2004, p. 594.
- [30] *Smithells Metals Reference Book*, Eight Edition. Eds.: Gale, W. F., Totemeier, T. C. Amsterdam, Elsevier 2004.
- [31] WANG, Y.—ZHANG, Z.—WANG, W.—BIAN, X.: *Mat. Sci. Eng.*, A366, 2004, p. 17.
- [32] MÁTHIS, K.—TROJANOVÁ, Z.: *Kovove Mater.*, 43, 2005, p. 238.
- [33] NEUBERT, V.—STULÍKOVÁ, I.—SMOLA, B.—BAKKAR, A.—MORDIKE, B. L.: *Kovove Mater.*, 42, 2004, p. 31.
- [34] WINZER, N.—ATRENS, A.—SONG, G.—GHALI, E.—DIETZEL, W.—KAINER, K. U.—HORT, N.—BLAWERT, C.: *Adv. Eng. Mater.*, 7, 2005, p. 659.
- [35] HADZIMA, B.—PALČEK, P.—CHALUPOVÁ, M.—ČANÁDY, R.: *Kovove Mater.*, 41, 2003, p. 257.